



# Paleogene buried landscapes and climatic aberrations triggered by mantle plume activity

Benedict W. Conway-Jones\*, Nicky White\*

Bullard Laboratories, Department of Earth Sciences, University of Cambridge, Madingley Rise, Madingley Road, Cambridge, CB3 0EZ, UK



## ARTICLE INFO

### Article history:

Received 5 January 2022

Received in revised form 11 April 2022

Accepted 24 May 2022

Available online xxxx

Editor: R. Bendick

### Keywords:

Icelandic plume

seismic reflection

hyperthermal events

PETM

## ABSTRACT

The Icelandic plume, a major mantle upwelling located beneath the North Atlantic Ocean, plays a dominant role in controlling periodic uplift of continental margins and of oceanographic gateways during Cenozoic times. Independent evidence shows that plume activity fluctuates on timescales of  $\leq 1$  Myr. Here, we describe and analyze a spectacular sequence of Paleogene buried landscapes imaged on seismic reflection surveys from the continental margin of northwest Europe. These transient landscapes recur on intervals of 2–3 Myrs, coincide with volcanic activity, and exhibit topographic relief of hundreds of meters. They probably represent the surficial expression of thermal fluctuations that spread radially away from the plume conduit. Five landscapes are coeval with global hyperthermal aberrations characterized by negative excursions of  $\delta^{13}\text{C}$  and by positive excursions of Fe intensity, which is a proxy for carbonate dissolution. We propose a causal relationship whereby thermal fluctuations of the mantle plume generate transient uplift and volcanic activity, which act to release significant quantities of greenhouse gases and thus trigger hyperthermal aberrations. A longer period oscillation of  $\delta^{13}\text{C}$  values is superimposed upon these aberrations that is attributable to a combination of silicate weathering and volcanic degassing caused by the interaction of plume activity and plate spreading.

© 2022 The Author(s). Published by Elsevier B.V. This is an open access article under the CC BY license (<http://creativecommons.org/licenses/by/4.0/>).

## 1. Introduction

It is generally agreed that a mantle convective upwelling centered beneath Iceland plays a role in generating and maintaining anomalous vertical elevations across the North Atlantic region (Fig. 1a). Throughout this region, present-day oceanic spreading ridges and plates are 1–2 km shallower than expected and fringing continental margins are elevated (White and McKenzie, 1989). Existence of a large mantle plume with a buoyancy flux of up to  $20 \text{ Mg s}^{-1}$  has been confirmed by regional seismic tomographic models which image a substantial and irregular-shaped negative shear-wave velocity anomaly beneath the lithospheric plates (e.g. Schoonman et al., 2017). There is interest in determining how the Icelandic plume has evolved through geologic time (White and McKenzie, 1989). The spatial and temporal distribution of Cenozoic magmatism suggests that this plume initiated at about 64 Myrs and that its planform rapidly expanded. At 55 Myrs, continental rifting and seafloor spreading accompanied large-scale basaltic magmatism triggered by decompression melting. Plume activity has also waxed and waned on shorter timescales. Com-

pelling evidence for fluctuating plume behavior relies on the fact that the plume is transected by a mid-oceanic ridge, which acts as a linear window into temporal variability of the underlying thermal structure. The resultant pattern of time-transgressive V-shaped ridges and troughs that straddle the Reykjanes Ridge south of Iceland enables a record of radial thermal fluctuations to be reconstructed (Parnell-Turner et al., 2014). These fluctuations are  $\pm 30^\circ\text{C}$  with a periodicity of 0(3–5) Myrs. Paleogene fluctuations are thought to have triggered periodic regional continental uplift and deposition of clastic submarine fans (White and Lovell, 1997). Mapping of three-dimensional (3D) seismic reflection surveys calibrated by borehole measurements reveals buried terrestrial landscapes that are sandwiched between marine strata. One dramatic example shows that rapid uplift and subsidence with an amplitude of 500–800 m occurred at  $55.80 \pm 0.50$  Myrs (Hartley et al., 2011). This scale of transient uplift cannot be reconciled with glacio-eustatic mechanisms. Instead, rapid uplift and subsidence are generated when an asthenospheric thermal anomaly spreading away from the center of the Icelandic plume is advected beneath the margin.

Here, we present evidence for an entire sequence of transient buried landscapes associated with coeval volcanism that developed during Paleogene times. These stratigraphically discrete landscapes are stacked upon each other, recording a succession of regional

\* Corresponding authors.

E-mail addresses: [bc477@cam.ac.uk](mailto:bc477@cam.ac.uk) (B.W. Conway-Jones), [njw10@cam.ac.uk](mailto:njw10@cam.ac.uk) (N. White).

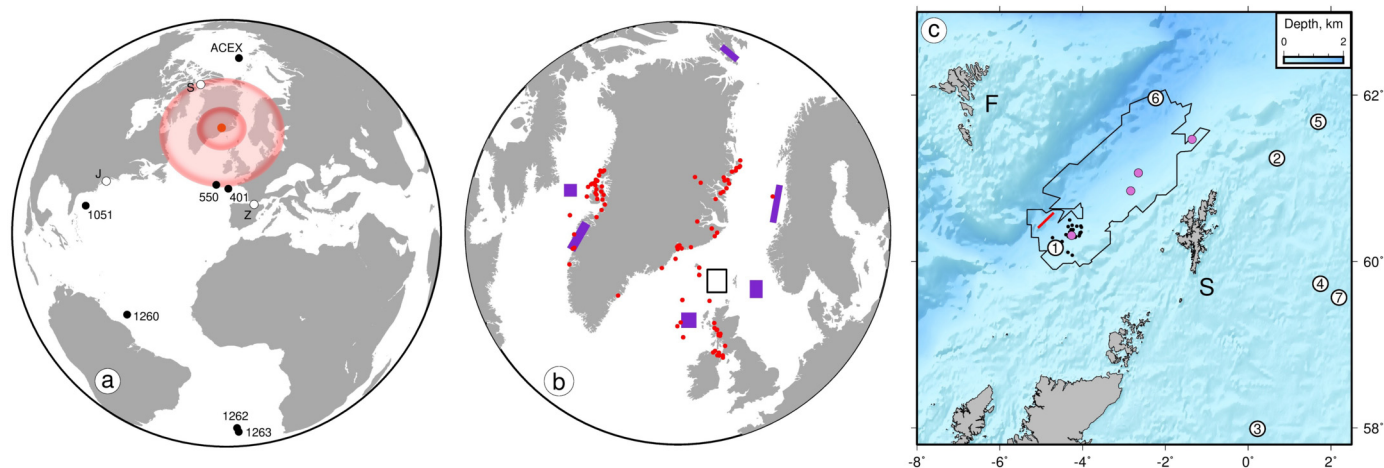


**Fig. 1. Plate reconstruction and borehole distribution.** (a) Global map showing plate reconstruction at 55 Myrs (azimuthal equidistant projection centered on 30°N, 15°W). Red circle = putative center of Icelandic plume at 55 Myrs (White and McKenzie, 1989); annular red shading = approximate extent of radial spreading of plume at 55 Myrs (Hartley et al., 2011); numbered black circles = relevant Ocean Drilling Program (ODP) sites; labeled white circles = locations of notable stratigraphic sites where J = New Jersey (Sluijs and Brinkhuis, 2009), S = Stenkul Fjord (Sudermann et al., 2021) and Z = Zumaia (Pujalte et al., 2014). (b) Regional map of North Atlantic Ocean showing plate reconstruction at 55 Myrs. Small red dots = distribution of magmatic samples used to construct probability density function shown in Fig. 6b (Wilkinson et al., 2017); black box = location of panel (c); purple boxes = locations of other ancient buried landscapes (Stucky de Quay et al., 2017; Stoker et al., 2012; Dam, 2002; Plink-Björklund and Steel, 2006; Dalhoff et al., 2003). (c) Bathymetric map of region, including Faroe-Shetland basin, that shows location of 3D seismic survey and boreholes (Mercator projection). Black polygon = location of 3D survey; black circles = loci of borehole checkshot surveys used to calculate time-depth relationship; numbered open circles = loci of boreholes used in Figs. 2 and 6d; pink circles = loci of index boreholes used to construct lithostratigraphic and biostratigraphic framework (Mudge and Bujak, 2001); thick red line = location of 2D vertical slice from 3D survey shown in Fig. 3; F = Faroe Islands; S = Shetland Islands. (For interpretation of colors in figure(s), the reader is referred to web version of article.)

uplift events that are thought to have been generated by the horizontal advection of thermal fluctuations beneath the lithospheric plate—an hypothesis that is corroborated by subsequent Neogene behavior of the Icelandic plume (Parnell-Turner et al., 2014). We explore the connections between five prominent landscapes and a series of paleoclimatic aberrations—the global hyperthermal events of Paleogene times. Our primary aim is to determine the extent to which there may be a genetic relationship between plume activity and transient landscape development and whether or not these events intrude upon the global climatic signal. Finally, we suggest that the combination of Icelandic plume activity and lithospheric rifting between Greenland and Northwest Europe triggered a longer period oscillation of Paleogene cooling and warming. This oscillation can be accounted for by regional silicate weathering during the initial stages of plume activity followed by a period of volcanic degassing when plume-generated magmatism increased during separation of the North American and Eurasian plates.

## 2. Stratigraphic unconformities and ancient buried landscapes

### 2.1. Regional framework

We describe a sequence of buried terrestrial landscapes that punctuate Cenozoic marine strata within the Faroe-Shetland basin (Fig. 1b). These landscapes were mapped on a 3D seismic reflection survey that covers  $2 \times 10^4$  km<sup>2</sup> (Appendix). This survey is calibrated with 36 boreholes, enabling lithologic, biostratigraphic and depositional constraints to be integrated with reflectivity mapping. The chronology of significant stratigraphic events is determined using a detailed regional biostratigraphic framework that has been recalibrated with respect to a modern orbitally tuned global timescale (Fig. 2; Speijer et al., 2020; Mudge and Bujak, 2001). This framework is based upon bioevents of dinoflagellate cysts, foraminifera, pollen, radiolaria and diatoms from four boreholes located along the axis of the Faroe-Shetland basin (Fig. 1c; Supplementary Information). Biostratigraphic analysis is primarily based upon conventional core and sidewall core material, supplemented by ditch cuttings.

The sedimentary basin was formed by Late Cretaceous lithospheric rifting followed by Cenozoic thermal subsidence (Shaw Champion et al., 2008). Paleogene stratigraphy is characterized by marine deposition that is interrupted by erosional unconformities, which are capped by terrestrial strata (Knox et al., 1997). We examine in detail four surfaces, Q–T, that were sub-aerially exposed, incised and rapidly buried. There is regional evidence for a fifth older surface which is not mappable within the Faroe-Shetland basin. On a single vertical slice through the seismic volume, these four stacked surfaces are manifest as irregular reflective surfaces (Fig. 3). Each surface was mapped by hand-picking in-lines and cross-lines (i.e. orthogonal vertical slices) with a resolution of ~30 m. Post-depositional folding is removed from unconformities Q and R by flattening the top surface of the Balder Formation and from unconformities S and T by flattening topset surfaces of the Stronsay delta. Depth conversion, decompaction and isostatic unloading were carried out using 29 borehole checkshot surveys (Appendix; Shaw Champion et al., 2008). These four landscapes reveal patterns of dendritic drainage characterized by over-steepened slopes and spurs that are typical of eroding landscapes where soft lithologies undergo rapid uplift (Fig. 4).

### 2.2. Landscape Q

The oldest Landscape Q initiated at  $59.15 \pm 0.45$  Myrs when an erosional unconformity cut into the underlying Vaila Formation. This formation comprises marine carbonate muds and sandstones (Figs. 2 and 3b; Knox et al., 1997). The pattern of erosional incision together with subsequent deposition of lignite are consistent with development of a fluvial landscape. The age of this important sequence boundary, which marks the top of the Vaila Formation, is biostratigraphically constrained by a marked change of the dominant dinocyst species from *Areoligera* cf. *coronata* and *P. pyrophorum* to *Areoligera gippingensis* (Mudge and Bujak, 2001). Immediately above this boundary, the agglutinated foraminifera *Reticulophragmium* cf. *garciassoi*, which is confined to Thanetian times, occurs. The exposure duration of Landscape Q is limited to  $\leq 2.5$  Myr since the short-lived *Alisocysta margarita* occurs immediately above and below the sequence boundary (Speijer et al., 2020).

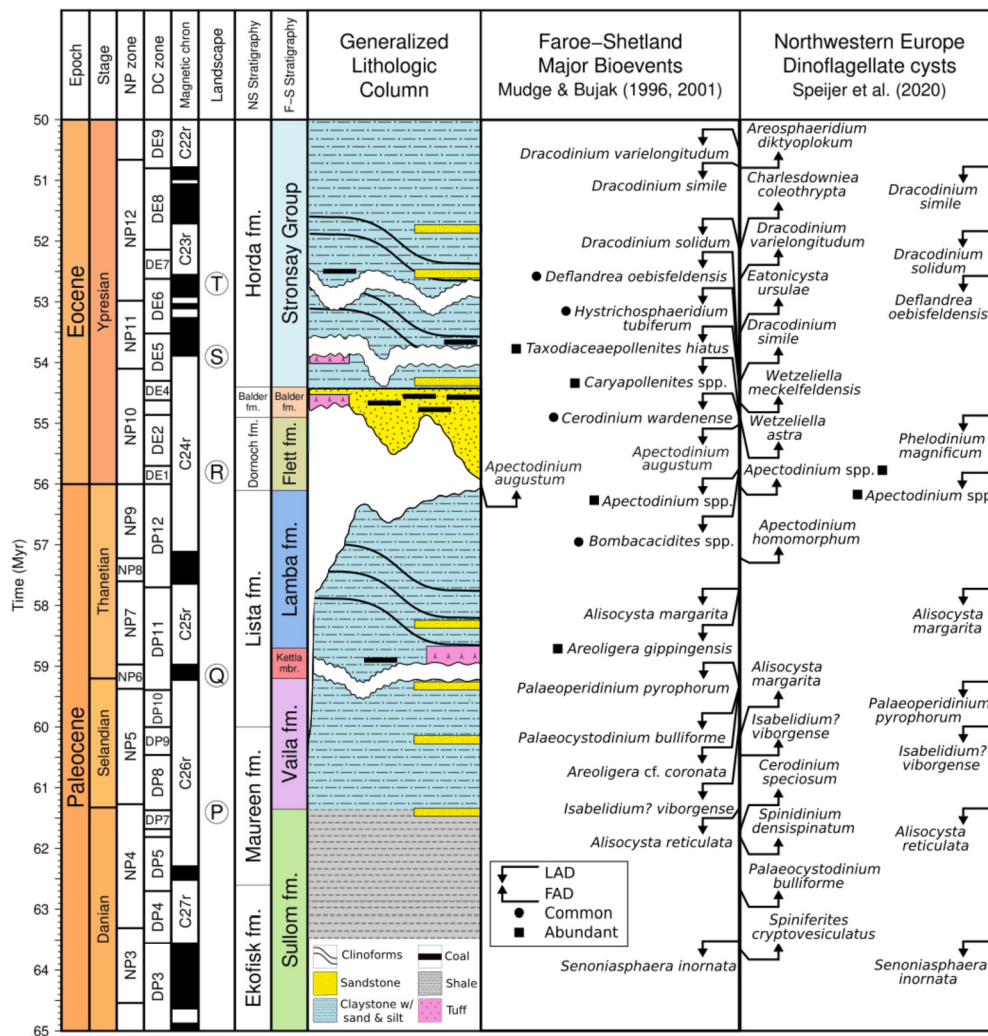


**Fig. 2. Paleocene to Early Eocene stratigraphic framework.** At left-hand side, absolute time scale, nannoplankton (NP) zonation, dinoflagellate cyst (DC) zonation, and magnetic polarity chronology taken from Speijer et al. (2020) and King (2016). Buried landscapes P, Q, R, S and T are shown in Fig. 4. NS and F-S refer to North Sea and Faroe-Shetland stratigraphies taken from Mudge and Bujak (1996), Knox et al. (1997) and Mudge and Bujak (2001). Stratigraphic column for generalized lithologic log is adapted from (Shaw Champion et al., 2008). At right-hand side, timings of major bioevents are modified from Mudge and Bujak (1996) and from Mudge and Bujak (2001) by tuning with respect to absolute timescale of Speijer et al. (2020) where LAD = last appearance datum and FAD = first appearance datum. Dinoflagellate cyst biostratigraphic framework is taken from Speijer et al. (2020).

This buried landscape is dominated by a major catchment with a prominent sinuous channel that has a relief of 310 m (Fig. 4a). Interlocking spurs occur within the higher reaches of this channel where steep tributaries are visible. Landscape Q is overlain by the Kettla Tuff Member of the Lamba Formation (Fig. 3; Knox et al., 1997). This tuff manifests a surge of volcanism associated with Phase 1 of the North Atlantic Igneous Province (White and McKenzie, 1989).

### 2.3. Landscape R

The overlying Lamba Formation comprises a prograding deltaic sequence that contains Thanetian agglutinated benthic foraminifera, notably *S. spectabilis* and *Reticulophragmium cf. garillasoi*, confirming the transient nature of Landscape Q (Knox et al., 1997). The upper boundary of this formation is the exquisitely preserved Landscape R, which initiated at  $55.80 \pm 0.8$  Myrs (Shaw Champion et al., 2008; Hartley et al., 2011). From a biostratigraphic perspective, this sequence boundary marks a dramatic shift from agglutinated benthic foraminifera to calcareous benthic foraminifera and diatom-restricted microfaunas (Mudge and Bujak, 2001). The short-lived *Apectodinium augustum*, which is characteristically abundant

at this boundary, defines the Thanetian-Ypresian transition at 56 Myrs (Fig. 2). Sub-aerial exposure of Landscape R lasted < 2 Myrs in accordance with the first and last appearance datums of *Apectodinium augustum* within the Flett formation, the common occurrence of *Cerodinium wardenense*, and the abundant occurrence of *Caryapollenites* spp. (Fig. 2; Mudge and Bujak, 2001; Speijer et al., 2020).

We revised and augmented the mapping of this landscape using additional seismic reflection surveys (Fig. 4b). It is bisected by a dramatic meandering channel, which has ~ 8 major tributary channels. The spatial pattern of knickzones along these channels delineates three peneplains at elevations of 200 m, 450 m and 750 m with reference to the base of the prominent paleo-seacliff (Supplementary Information). Landscape R has a relief of 500–750 m. It is infilled by the Flett Formation, which is a terrestrial unit containing lignite beds and pollen assemblages dominated by *Bombacacidites* and *Caryapollenites* (Fig. 3; Mudge and Bujak, 2001). This formation is overlain by tuffs and mudstones of the Balder Formation, heralding a rapid return to marine conditions (Fig. 3; Knox et al., 1997). An equivalent landscape is recognized in the North Sea basin (Stucky de Quay et al., 2017).



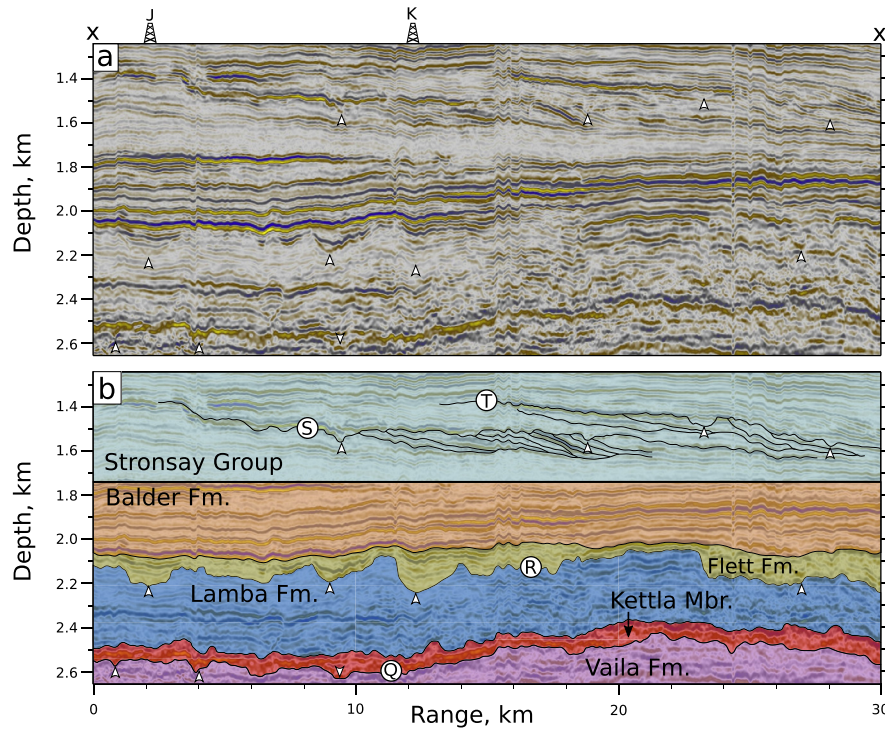


**Fig. 3. Vertical slice through seismic volume.** (a) 2D vertical slice through 3D seismic reflection survey where Top Balder surface (54.8 Myrs) is flattened for clarity. Red/blue wiggles = reflections with positive/negative polarity; sequences of white arrows indicate loci of four principal incised surfaces described in text; labeled drilling rig icons = projected loci of two boreholes used for stratigraphic correlation where J = 204/16-1 and K = 204/17-1. (b) Geologic interpretation of panel (a). Labeled colored polygons = Paleogene stratigraphic units; thick black lines = principal lithological boundaries and incised surfaces; thin black lines = deltaic foreset deposits that lie beneath top two incised surfaces; encircled letters = four incised surfaces shown in Fig. 4.

#### 2.4. Landscapes S and T

The lower part of the overlying Stronsay Group comprises ~ 100 m-high northward prograding clinoformal surfaces dominated by marine sandstones and mudstones (Fig. 3). Upper surfaces of two deltas have rugose geometries that constitute landscapes S and T (Fig. 4c and d). Both landscapes are overlain by lignite fragments, by carbonaceous material, and by tuffs, indicative of sub-aerial exposure with coeval volcanism. A combination of the first appearance datum of *Dracodinium simile* within underlying strata and last appearance datums of *Homotrybium tenuispinosum* and *Dracodinium politum* within overlying strata shows that this pair of landscapes developed between 54.3 and 51.7 Myrs (Speijer et al., 2020). In the adjacent Rockall basin, Stoker et al. (2012) document the existence of two sub-aerially exposed unconformities that correspond to landscapes S and T. The stratigraphic section that spans both unconformities correlates with nannoplankton zone NP10 and with lowermost NP12, based upon the combined presence of *Adnatosphaeridium multispinosum*, *Adnatosphaeridium robustum*, *Achilleodinium biformoides*, *Achomosphaera alcornu*, *Homotrybium tenuispinosum* and *Wetzeliella* spp. Significantly landscapes S and T and their temporal equivalents in the Rockall basin are separated by occurrences of *Deflandrea oebisfeldensis*, which has a last appearance datum of ~53 Myrs. Thus, it is safe to conclude that Landscape S was incised between 54.3 and 53.0 Myrs and that Landscape T was incised between 53.0 and 51.7 Myrs. Landscape S is characterized by a large canyon with steep slopes above which lies an extensive peneplain (Fig. 4c). This canyon is 25 km long and cuts down into prograding clinoformal surfaces of the underlying deltaic deposits (Fig. 3). Minor catchments occur along the eastern escarpment. Landscape T is characterized by a series of catchments that are distributed along a 15 km-long northeast-facing slope (Fig. 4d).

#### 2.5. Regional context

We contend that the degree of exquisite detail recorded by these preserved landscapes and recovered by 3D seismic reflection surveying is remarkable. The causes of this unprecedented degree of preservation are threefold. First, these landscapes developed within a paleoenvironmental Goldilocks zone which enhanced their preservation potential. If pre-existing water depths had been greater than several hundred meters, it is unlikely that this continental margin would have been sub-aerially exposed at all. If, on the other hand, pre-existing water depths had been negligible, more prolonged sub-aerial exposure would have given rise to wholesale peneplanation. Secondly, regional uplift was short-lived, which means that these transient landscapes were rapidly submerged. Thirdly, subsequent sedimentation rates were rapid so that submarine erosion did not occur (Supplementary Information). This particular combination of water depth, transient uplift and sedimentation rate has ensured preservation of these delicately sculpted surfaces.

Fragmentary evidence supports the existence of these four buried landscapes throughout the North Atlantic region (Fig. 1a). However, erosional surfaces are often featureless peneplains where only the deepest incised structures are locally preserved. For example, in the Paris basin a 6–7 Myr hiatus between Thanetian sedimentary rocks of the Chalons sur Vesles and Moulin Compensé formations and underlying Danian chalk deposits has been linked to a regional uplift event that coincides with Landscape Q (Gale and Lovell, 2020). In southern England, a similar hiatus occurs between the Thanet Formation and Late Cretaceous deposits where ~ 500 m of chalk are absent. However, both hiatuses are too protracted to make definitive correlations. In the Kangerlussuaq basin of East Greenland, the Vandfaldsdalen Formation, consisting of pillow basalts and hyaloclastites, is overlain by lava flows with oxidized surfaces, implying a transition from submarine to sub-aerial

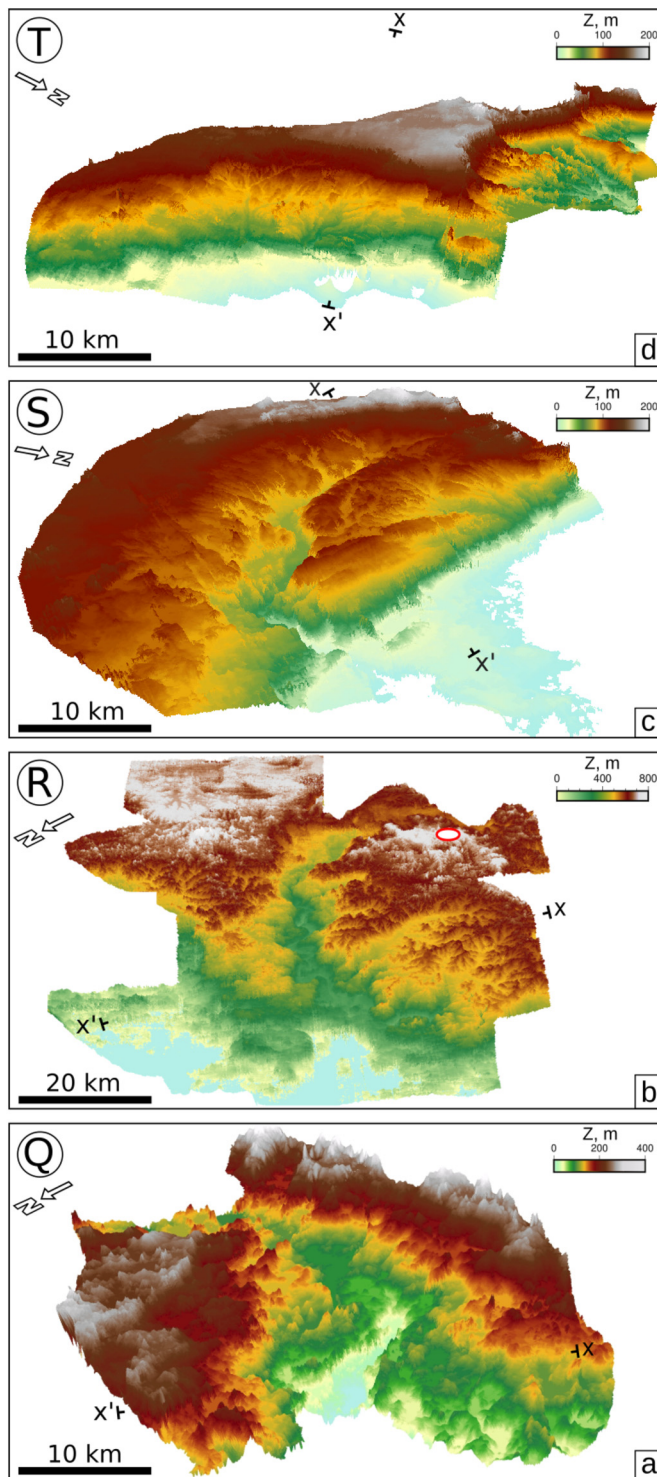


**Fig. 4. Four ancient buried landscapes.** (a) Perspective view of buried Landscape **Q** which is 59.15 Myrs.  $x-x'$  indicates orientation of vertical slice shown in Fig. 3. (b)–(d) Same for **R**, **S** and **T** which are 55.80 Myrs, 53.90 Myrs and 52.70 Myrs, respectively. White circle in panel (b) = location of borehole 1 (Fig. 1).

conditions that is coeval with Landscape **Q** (Brooks, 2011). Burgeoning evidence supports the regional extent of Landscape **R**. For example, a deeply incised erosional surface lies beneath the Harwich formation of the London basin (King, 2016). Here, the estuarine Blackheath Formation records a return to marine conditions by ~55 Myrs. This major sequence boundary is one of a number of erosional surfaces that occur throughout southern England at

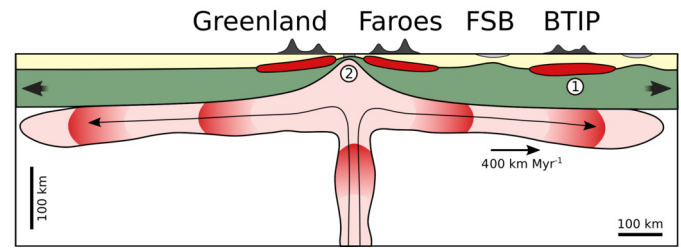


**Fig. 5. Icelandic plume at 55 Myrs.** Scaled cartoon showing proposed geometry of Icelandic plume and configuration of rifting continental plates at 55 Myrs. Pink shading = extent and internal structure of plume showing migration of hotter blobs of mantle material up plume conduit and into plume head (shapes of blobs reflect radial Poiseuille flow); yellow/green shading = continental crust/lithospheric mantle; red slugs at base of crust = stylized distribution of magmatic underplating; dark gray triangles = stylized distribution of surficial volcanism; gray bowl-shaped polygons = sedimentary basins; encircled numbers = phases of North Atlantic Igneous Province activity referred to in text; black arrows = plate spreading vectors; FSB = Faroe-Shetland basin; BTIP = British Tertiary (i.e. Cenozoic) Igneous Province.

this time. Coeval erosional surfaces are recognized along the Norwegian and Greenland continental margins and on the fringes of the Jan Mayen microcontinent (see, e.g., Ren et al., 2003; Storey et al., 2007; Dalhoff et al., 2003). There is widespread evidence supporting the existence of landscapes **S** and **T**. In the Kortrijk region of Belgium, the boundary between the Upper and Lower Roubaix Clay Formation is a marked erosional surface that represents relative sea-level fall (Steurbaat and King, 2017). This boundary is correlated with the deeply incised base of the Portsmouth Member of the Hampshire basin and it is coeval with Landscape **T**. Coastal outcrops along Van Keulenfjorden of Spitsbergen preserve slope deposits of the Batfjellet Formation onto which landscapes are sculpted and then overlain by the Aspelintoppen Formation (Plink-Björklund and Steel, 2006). The stratigraphic setting, morphology and estimated duration suggest that these landscapes are coeval with **S** and **T**. Sudermann et al. (2021) describe a stratigraphic succession at Stenkul Fiord of Ellesmere Island where a volcanic ash band with a U/Pb age of  $53.7 \pm 0.06$  Myrs lies close to an unconformity.

Finally, there is fragmentary field evidence for an erosional surface that precedes Landscape **Q**. For example, Dam (2002) describes an unconformity associated with sub-aerial exposure in the Nuussuaq region of West Greenland (Landscape **P**). Terrestrial sandstones of the Paatuutkløften Formation cut down into marine mudstones of the mid-Danian Tupaasat Formation by ~200 m. These Paleogene strata were buried and compacted by ~2 km of overburden. In order to estimate the original relief of this buried landscape, we assume an initial porosity of 0.5 and a compaction decay length of 2.5 km which yields a corrected relief of  $280 \pm 10$  m. This terrestrial surface was subsequently buried by hyaloclastic deposits that are coeval with a volcanic deposit with an  $^{40}\text{Ar}/^{39}\text{Ar}$  date of 60.9–61.3 Myrs (Dam, 2002). Fragments of Landscape **P** are distributed throughout the North Atlantic region. Larsen et al. (1999) describe a correlative unconformity from the Kangerlussuaq basin (Dam, 2002). Offshore West Greenland, a Danian-Selandian unconformity occurs between the Markland and Cartwright formations.

### 3. Global hyperthermal aberrations

#### 3.1. Transient activity of Icelandic plume

The scale and periodicity of regional uplift associated with these multiple buried landscapes suggest that they are generated by thermal fluctuations which spread away the center of the Icelandic mantle plume (Parnell-Turner et al., 2014). When a thermal fluctuation advects horizontally beneath the fringing continental



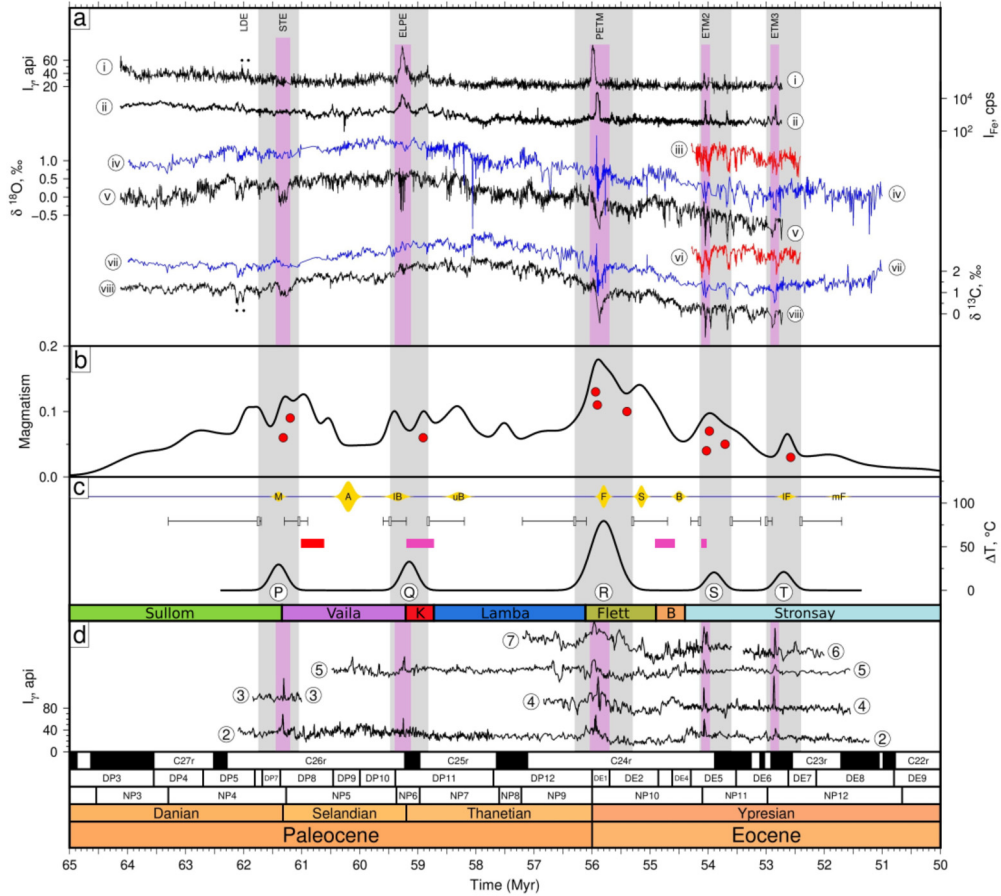


**Fig. 6.** Transient uplift episodes and global hyperthermal events. (a) Proxy records from ODP sites. i = Gamma ray intensity record (Shipboard Scientific Party, 2004); ii = Fe intensity record (Barnet et al., 2019); iii–v and vi–viii =  $\delta^{18}\text{O}$  and  $\delta^{13}\text{C}$  records where red/blue/black lines refer to sites 1263/1209/1262 (Lauretano et al., 2015; Westerhold et al., 2018; Barnet et al., 2019); gray polygons = transient uplift episodes; labeled pink polygons = significant hyperthermal events; (b) Probability density function showing volcanic activity of North Atlantic Igneous Province (Wilkinson et al., 2017). Red circles = highest quality Ar/Ar and U/Th radiometric dates. (c) Colored bar = stratigraphy of Faroe-Shetland basin (see Fig. 2; black line = calculated asthenospheric temperature anomalies (Fig. 4, Dam, 2002); red boxes = volcanic deposits; encircled letters = buried landscapes; gray rectangles with lines = uncertainties of start/end of transient episodes; yellow polygons = clastic fans scaled by volume (M = Maureen, A = Andrew, IB = lower Balmoral, uB = upper Balmoral, F = Forties, S = Sele, B = Balder, IF = lower Frigg, mF = middle Frigg; White and Lovell, 1997); blue lines = mud deposition. (d) Borehole gamma ray records (see Fig. 1b for borehole locations).

margins, a phase of transient uplift is generated (Figs. 1 and 5; Rudge et al., 2008). Isostatic arguments show that regional uplift,  $U$ , generated by a thermal fluctuation,  $\Delta T$ , is given by

$$U = \frac{2h\alpha\Delta T}{1 - \alpha T_o} \quad (1)$$

where  $2h$  is thickness of the asthenospheric channel,  $\alpha = 3.28 \times 10^{-5} \text{ } ^\circ\text{C}^{-1}$  is thermal expansion coefficient, and  $T_o = 1400 \text{ } ^\circ\text{C}$  is ambient temperature of the plume (Appendix; Rudge et al., 2008). Tomographic models suggest that  $2h = 150 \pm 50 \text{ km}$  (Schoonman et al., 2017). The amplitude of uplift recorded by a landscape yields an estimate of  $\Delta T$  (Fig. 6c). From Equation (1), we obtain  $\Delta T$  values of  $33^{+16}_{-8}$ ,  $80^{+40}_{-20}$ ,  $21^{+10}_{-5}$  and  $21^{+11}_{-5} \text{ } ^\circ\text{C}$  for landscapes Q, R, S and T, respectively. Landscape P has a  $\Delta T$  value of  $30^{+15}_{-7} \text{ } ^\circ\text{C}$ .

Three of these estimates are consistent with the results of Parnell-Turner et al. (2014), who analyzed Neogene V-shaped ridges and obtained temperature fluctuations of  $25\text{--}30 \text{ } ^\circ\text{C}$  that varied on timescales of 3–8 Myrs. The obvious exception is the  $\Delta T$  value for Landscape R, which predates V-shaped ridge activity and reflects an earlier hotter stage of the Icelandic plume (White and McKenzie, 1989). The timings of transient landscape development also align with peaks of magmatism (Fig. 6b and c). Recurrence of these transient landscapes gives rise to discrete phases of denudation and submarine fan deposition (White and Lovell, 1997). Here,

episodes of fan deposition described by Neal (1996) have been calibrated with the astronomical timescale (Appendix; Speijer et al., 2020). There is a close relationship between timing of these clastic deposits, magmatic peaks, volcanic tuff deposits, and landscapes (Fig. 6c). For example, landscapes P and Q coincide with deposition of the Maureen and Lower Balmoral fans while landscapes R and T coincide with the Forties and Lower Frigg fans. In each case, the scales of regional uplift and of fan volume are proportional. Fan deposition is absent at distal boreholes of the Faroe-Shetland basin, where sedimentation is dominated by mudstones, which exhibit discrete spikes of gamma ray intensity that are coeval with individual landscapes (Appendix). If sedimentary composition is relatively uniform, these spikes may be indicative of a relative increase in terrestrially sourced material enriched by radioactive elements or of an organic bloom generated by enhanced erosion and delivery of nutrients. Another well-known mechanism that can trigger such spikes is an increase in carbonate dissolution triggered by a reduction in the carbonate saturation state through the rapid addition of  $\text{CO}_2$ .

### 3.2. Plume activity and climatic aberrations

We now consider the relationship between buried landscapes, mantle plume behavior and global climatic aberrations. The Paleogene period is characterized by climatic perturbations known

as hyperthermal events that are superimposed upon a longer term oscillation of cooling and warming (Fig. 6a; Zachos et al., 2001). The most pronounced event is the Paleocene-Eocene Thermal Maximum (PETM), which occurs at  $55.9 \pm 0.1$  Myrs. Other significant events include the Danian/Selandian Transition Event (STE at  $61.3 \pm 0.15$  Myrs), the Early Late Paleocene Event (ELPE at  $59.25 \pm 0.1$  Myrs) and two Eocene Thermal Maximum events (ETM2 and ETM3 at  $53.9 \pm 0.05$  Myrs and  $52.85 \pm 0.08$  Myrs, respectively; Barnet et al., 2019). These aberrations are manifest as global perturbations of  $\delta^{13}\text{C}$  and of Fe intensity, which is diagnostic of increased clay fraction as a consequence of enhanced carbonate dissolution (Röhl et al., 2003; Fig. 6a). At ODP borehole 1262, spikes of Fe intensity,  $I_{\text{Fe}}$ , and of gamma ray intensity,  $I_{\gamma}$ , linearly correlate with a coefficient of determination of  $R^2 = 0.96$  such that  $I_{\text{Fe}} = 413 I_{\gamma}$ . These spikes coincide with negative marine excursions of  $\delta^{13}\text{C}$  that are up to 2.5‰, although excursions of up to 8‰ have been recorded by other ancient archives (see Table 1 of McInerney and Wing, 2011).

Osmium isotopic records, mercury concentrations and radiometrically dated volcanic rocks from the continental fringes of the North Atlantic Ocean reveal an excellent temporal coherence between the North Atlantic Igneous Province (NAIP) and the PETM event (Storey et al., 2007; Dickson et al., 2015; Jones et al., 2019a). This coherence suggests that basaltic magmatism, generated by fluctuations of the Icelandic plume, is a trigger for significant addition of  $^{13}\text{C}$ -depleted carbon to surficial reservoirs during the PETM event. However, the composition and origin of carbon species is much debated. We note that the volume of magmatism associated with the NAIP is sufficient to account for the volume of carbon but that positive feedback effects can also amplify climatic change (Gutjahr et al., 2017; Jones et al., 2019b). Analysis of an inventory of hydrothermal vents along the Norwegian continental margin suggests that methane generated by contact metamorphism could have been a primary source of carbon (Svensen et al., 2004; Frieling et al., 2016). Regional uplift and disruption to oceanic circulation could also be associated with methane release triggered by dissociation of gas hydrate deposits (Bice and Marotzke, 2002).

Reconciling the short (i.e.  $\sim 200$  ka) duration of the PETM event with the duration of NAIP volcanism is regarded as challenging (Storey et al., 2007). It is straightforward to estimate the transit time of a thermal fluctuation that horizontally advects beneath a lithospheric plate by considering what happens when a V-shaped ridge forms at a mid-oceanic ridge. At the present day, the axial length of the actively forming V-shaped ridge is  $100 \pm 50$  km (Parnell-Turner et al., 2014). The geometry of this migrating V-shaped ridge shows that the thermal fluctuation travels at a speed of  $282 \pm 24$  km/Myr, yielding a duration of  $350 \pm 180$  ka. Indirect evidence suggests that Paleogene thermal fluctuations traveled at greater speeds of up to 500 km/Myr (Rudge et al., 2008). We conclude that transient uplift events of sufficiently short duration can easily be generated by time-dependent mantle processes. Emission-based modeling of NAIP activity implies that it is capable of generating appropriate volumes of greenhouse gases on timescales of  $O(100)$  ka (Jones et al., 2019b).

Despite compelling evidence that the NAIP played a significant role in triggering the PETM event, volcanic events have not previously been invoked for other Paleogene hyperthermal aberrations. A probability density function of primarily  $^{40}\text{Ar}/^{39}\text{Ar}$  dates shows that there is a clear temporal correlation between NAIP magmatic activity, initiation of buried landscapes and perturbations of both stable isotopic and Fe intensity records (Wilkinson et al., 2017). Warm climatic excursions triggered by glacio-eustatic fluctuations cannot account for these observations since this association is not logically compatible with the relative sea-level falls required to generate emergent landscapes. Instead, borehole records confirm

a temporal link between episodes of regional uplift and hyperthermal aberrations (Fig. 6a and d). For example, peak intensities of Fe and gamma ray records for hyperthermal events at ODP site 1262 coincide with, and are proportional to, landscape relief (Fig. 7d and e). A useful proxy for the size of a hyperthermal event is the carbon isotope excursion,  $\delta^{13}\text{C}_f - \delta^{13}\text{C}_i$ , that is used to estimate the mass of added carbon,  $M$ , where

$$M = \left( \frac{\delta^{13}\text{C}_f - \delta^{13}\text{C}_i}{\delta^{13}\text{C}_f - \delta^{13}\text{C}_+} \right) M_i. \quad (2)$$

$\delta^{13}\text{C}$  is the carbon isotopic ratio of each pool where subscripts  $i =$  initial,  $+$  = added, and  $f =$  final (McInerney and Wing, 2011). The initial mass of carbon,  $M_i = 5 \times 10^4$  Pg, and  $\delta^{13}\text{C}_i \approx 1\text{‰}$  (Fig. 6a). The value of  $\delta^{13}\text{C}_+$  varies between  $-6.6\text{‰}$  and  $-17\text{‰}$  with an average value of  $-11\text{‰}$  (Gutjahr et al., 2017). Given that mantle-derived carbon has a  $\delta^{13}\text{C}$  value of about  $-6\text{‰}$ , a composite carbon source is required. Methane is probably a significant contributor that could have been generated by melting of clathrate deposits or by contact metamorphism adjacent to hydrothermal vents (Svensen et al., 2004). We estimate  $M$  for the five hyperthermal events by assuming that  $\delta^{13}\text{C}_+ = -11^{+4.4}_{-6.0}\text{‰}$ . For the PETM and ETM2 events, we obtain values of  $1.01^{+0.59}_{-0.34} \times 10^4$  Pg and  $5.34^{+3.43}_{-1.86} \times 10^3$  Pg, respectively. These values are consistent with independent estimates of  $1.02 \pm 0.2 \times 10^4$  Pg and  $3.2 \pm 0.6 \times 10^3$  for the PETM and ETM2 events, respectively (Gutjahr et al., 2017; Harper et al., 2020). With the exception of the ELPE event, which in marine records is characterized by minor excursions of  $\delta^{13}\text{C}$ , landscape relief is proportional to added mass of carbon (Fig. 7d and e). Onshore records show that the ELPE event is often characterized by a more significant excursion of  $\delta^{13}\text{C}$  (Coccioni et al., 2019). Our results suggest that at least some hyperthermal events are associated with, and probably triggered by, transient plume activity. We propose that pulses of basaltic volcanism serve both as sources of  $\text{CO}_2$  and as triggers for methane release.

### 3.3. Long-period oscillation

The best-known hyperthermal events clearly fall within a long period oscillation of  $\delta^{13}\text{C}$  values (Fig. 7a). This oscillation starts with a positive excursion, which has a peak value of  $\delta^{13}\text{C} = +2.4\text{‰}$  at 58 Myrs, and ends with a negative excursion, which has a peak value of  $\delta^{13}\text{C} = -0.3\text{‰}$  at 53.5 Myrs. We model the oscillation using a mass balance equation, based upon the combined production and decay of silicate weathering and volcanic outgassing, so that

$$\delta^{13}\text{C}(t) = \frac{M_i \delta^{13}\text{C}_i + c_v(t) \delta^{13}\text{C}_v + c_s(t) \delta^{13}\text{C}_s}{M(t)}. \quad (3)$$

In this equation,  $M_i$  and  $M(t)$  are initial and remaining masses of carbon within the surface reservoir where  $M_i$  is assumed to be  $5 \times 10^4$  Pg (McInerney and Wing, 2011).  $\delta^{13}\text{C}_i$ ,  $\delta^{13}\text{C}_v$  and  $\delta^{13}\text{C}_s$  are values of  $\delta^{13}\text{C}$  for the initial surface reservoir, for volcanic outgassing, and for silicate weathering, respectively (Table 1).  $c_s(t) = (\sigma \sqrt{2\pi})^{-1} F_s c(t)$  and  $c_v(t) = (\sigma \sqrt{2\pi})^{-1} F_v c(t)$  are carbon contributions to the surface reservoir as a function of time for silicate weathering and volcanic outgassing, respectively.  $F_s$  and  $F_v$  are appropriate scaling factors of opposite sign. The functions  $c_s(t)$  and  $c_v(t)$  are derived in the Appendix.

An important assumption of this calculation is that peak production of silicate weathering and of volcanism are temporally displaced (Fig. 7b). This assumption is justified by two significant observations. The first phase of plume-related magmatism is focused beneath the British Isles and beneath Greenland between

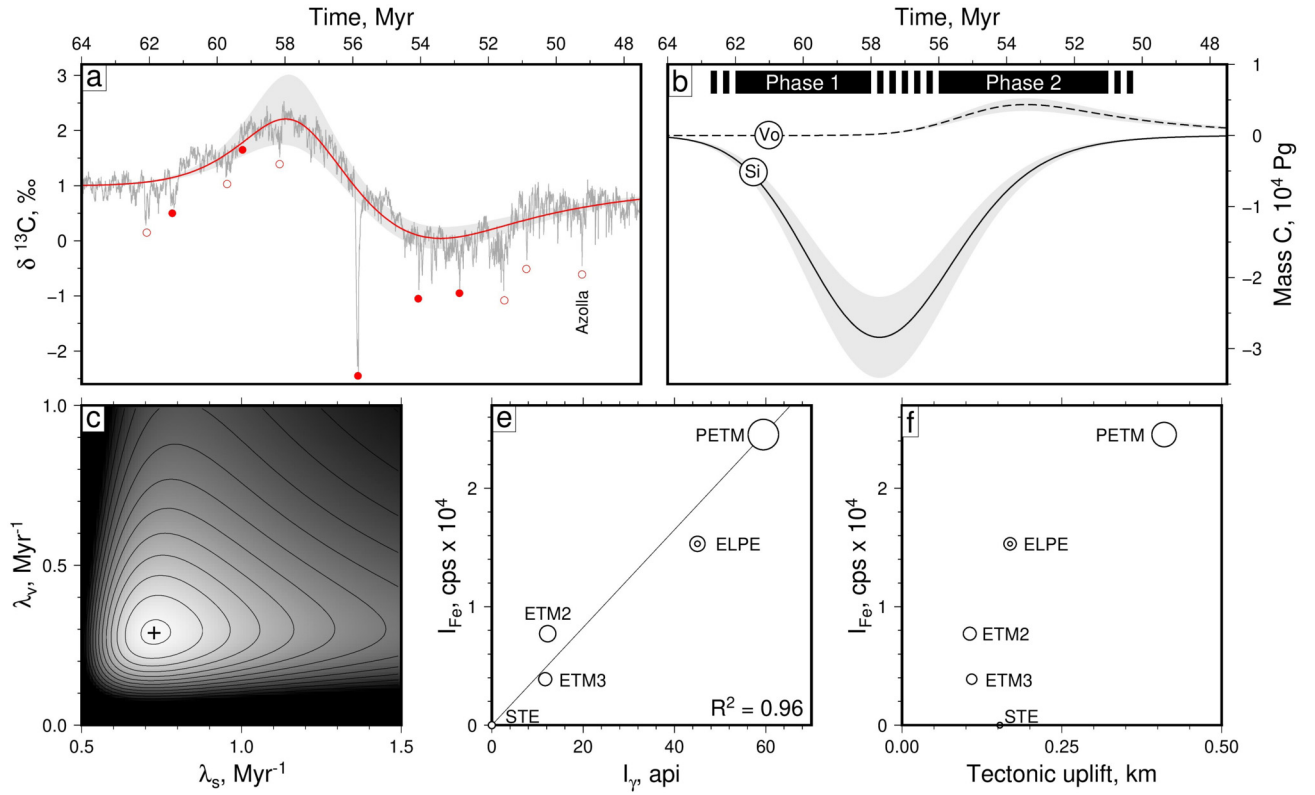


**Fig. 7. Observed and calculated carbon isotopic records.** (a) Gray line = observed concentration of  $\delta^{13}\text{C}$  as function of time (Westerhold et al., 2020); red line with gray band = calculated concentration of  $\delta^{13}\text{C}$  and its uncertainty as function of time; solid red circles = aberrations with negative spikes of  $\delta^{13}\text{C}$  that are coeval with five buried landscapes; open red circles = other notable aberrations with negative spikes of  $\delta^{13}\text{C}$ . (b) Black line labeled 'Si' = calculated production and decay of C caused by drawdown associated with silicate weathering; dashed line labeled 'Vo' = calculated production and decay of C caused by volcanic degassing; labeled black rectangles = phases of NAIP activity (White and McKenzie, 1989). (c) Root-mean-square (RMS) misfit as function of  $\lambda_s$  and  $\lambda_v$ . Black cross = locus of global minimum. (d) Empirical relationship between excursions of Fe intensity and excursions of Gamma ray intensity for five hyperthermal events. Labeled circles with error bars = hyperthermal events and uncertainties where diameters are proportional to calculated input masses of C (STE =  $2311^{+1313}_{-764}$  Pg, ELPE =  $1832^{+917}_{-572}$  Pg, PETM =  $10057^{+5876}_{-3365}$  Pg, ETM2 =  $5338^{+3433}_{-1857}$  Pg, ETM3 =  $4305^{+2818}_{-1508}$  Pg); black line = best-fitting line. Note that associated uncertainties are smaller than circle diameters and that small/large nested circles for ELPE represent marine/terrestrial carbon isotopic excursions, respectively. (e) Relationship between Fe intensity spike and amplitude of transient uplift episode for each hyperthermal event.

**Table 1**

Parameter values used to calculate carbon isotopic record with Equations (D.3) and (D.4).

Symbol	Description	Value	Independent estimate
$\delta^{13}\text{C}_i$	$\delta^{13}\text{C}$ of initial surface reservoir	1‰	$1 \pm 0.3\text{‰}^a$
$\delta^{13}\text{C}_v$	$\delta^{13}\text{C}$ for volcanic outgassing	-11‰	$-11^{+4.4}_{-6}\text{‰}^b$
$\delta^{13}\text{C}_s$	$\delta^{13}\text{C}$ for silicate weathering	0‰	
$t_{ov}$	Peak of magmatism	55.0 Myrs	$53.5 \pm 2$ Myrs <sup>c</sup>
$t_{os}$	Peak of silicate weathering	58.8 Myrs	$58 \pm 2$ Myrs <sup>d</sup>
$\sigma_v$	Standard deviation for magmatism	1.44 Myr	$1.25 \pm 0.5$ Myr <sup>c</sup>
$\sigma_s$	Standard deviation for weathering	1.89 Myr	$1.5 \pm 0.5$ Myr <sup>d</sup>
$\lambda_v$	Decay constant for magmatism	$0.288 \text{ Myr}^{-1}$	$4.2 \pm 1.6 \text{ Myr}^{-1e}$
$\lambda_s$	Decay constant for weathering	$0.727 \text{ Myr}^{-1}$	
$F_v$	Cumulative contribution of magmatism	$8.38 \times 10^3 \text{ Pg}$	$9.5^{+2.5}_{-2.3} \times 10^3 \text{ Pg}^f$
$F_s$	Cumulative contribution of weathering	$-1.15 \times 10^5 \text{ Pg}$	$-0.78^{+0.34}_{-0.34} \times 10^5 \text{ Pg}^d$

a = Westerhold et al. (2020); b = Gutjahr et al. (2017); c = White and McKenzie (1989); d = Jones et al. (2002); e = Colbourn et al. (2015); f = White et al. (2008).

64 and 57 Myrs (White and McKenzie, 1989). During this phase, regional uplift generated by large-scale magmatic underplating caused widespread regional erosion (White and Lovell, 1997; Jones et al., 2002). The resultant surge of silicate weathering was accompanied by minimal volcanic outgassing and triggered a global drawdown of carbon that generated a positive excursion of  $\delta^{13}\text{C}$ . This drawdown could have been amplified by enhanced burial of organic matter. The second phase of magmatism is almost exclusively focused along the axis of plate separation, which had two

significant consequences— melt production rate increased by several orders of magnitude as a result of rapid adiabatic decompression and regional uplift was negligible as a result of lithospheric thinning and oceanic plate formation (Storey et al., 2007). The consequent volcanic outgassing was accompanied by negligible regional erosion and triggered a negative excursion of  $\delta^{13}\text{C}$ .

To fit the positive excursion of  $\delta^{13}\text{C}$ ,  $F_s = 1.15 \times 10^5 \text{ Pg}$  and  $\lambda_s = 0.727 \text{ Myr}^{-1}$ . Significantly, this value of  $F_s$  is consistent with  $0.78^{+0.34}_{-0.34} \times 10^5 \text{ Pg}$  obtained by assuming  $3\text{--}6 \times 10^5 \text{ km}^3$  of sili-



ciclastic sediment with a density of  $2.65 \pm 0.2 \text{ Mg m}^{-3}$ , was weathered from the continents and deposited offshore (Jones et al., 2002). We also assume that 1 mole of carbon is sequestered for every mole of silicate mineral that is weathered. One consequence of large volumes of carbon being sequestered is a  $\sim 50\%$  loss from the surface reservoir, in agreement with studies suggesting that there was a  $\sim 50\%$  drop in atmospheric  $\text{CO}_2$  between 60 and 55 Myrs (Beerling and Royer, 2011). The value of  $\lambda_s$  implies it would take more than 1 Myr to replace carbon sequestered by silicate weathering, an order of magnitude greater than modern estimates (Hilton and West, 2020).

To fit the negative excursion of  $\delta^{13}\text{C}$ ,  $F_v = 8.38 \times 10^3 \text{ Pg}$  and  $\lambda_v = 0.288 \text{ Myr}^{-1}$ . This value of  $F_v$  is consistent with an estimate of  $9.5^{+2.5}_{-2.3} \times 10^3 \text{ Pg}$  obtained from the volume of extrusive magmatism seismically imaged along the margins of the North Atlantic Ocean (White and McKenzie, 1989; White et al., 2008). The erupted volume over a period of  $\sim 2$  Myrs is typically  $380 \pm 20 \text{ km}^2$  per kilometer, which is distributed along both margins over a strike length of 2500 km. These values yield an extrusive melting rate of  $0.95 \pm 0.05 \text{ km}^3 \text{ a}^{-1}$  at 55.0 Myrs, which is slightly less than that obtained by Storey et al. (2007). We assume that volcanic degassing from extrusive magmas emits  $5 \pm 1 \text{ kg m}^{-3}$  (Gutjahr et al., 2017). The value of  $\lambda_v$  implies that it would take more than 1 Myr to remove emitted carbon from the ocean-atmosphere system. Independent estimates of  $\lambda_v$  range from 2 to 5  $\text{Myr}^{-1}$  (Colbourn et al., 2015). Note that at the peak of silicate weathering, we assume that the extrusive melting rate is one order of magnitude smaller. This assumption is in accordance with an average extrusive melting rate of  $\sim 0.05 \text{ km}^3 \text{ a}^{-1}$  estimated from the spatial distribution of basaltic rocks on the British Isles and Greenland (White and McKenzie, 1989).

We acknowledge that this calculation is speculative and is predicated upon small values of  $\lambda_s$  and  $\lambda_v$  (Fig. 7c). Nevertheless, the resultant fit between observed and calculated oscillation is compelling (Fig. 7a). It implies that plume-related silicate weathering and volcanic outgassing act to moderate  $\delta^{13}\text{C}$  values between 64 and 48 Myrs.

#### 4. Conclusions

There is considerable interest in developing a quantitative understanding of rapid climatic changes within the geologic record. In recent decades, this understanding has been predicated upon the astronomical framework of orbital cyclicity. However, there are notable aberrations and exceptional trends that cannot easily be accounted for by this framework. During Paleogene times, for example, global hyperthermal events that are superimposed upon a longer period climatic oscillation occur, neither of which have obvious explanations. These events are of particular importance because they are regarded as ancient analogues of present-day climate change. One of the best known is the PETM event, which represents  $\sim 5^\circ \text{ C}$  of global warming with an associated carbon release of up to  $1.3 \times 10^4 \text{ Pg}$  over  $2 \times 10^4$  years (McInerney and Wing, 2011).

Mantle convective processes and volcanism are often proposed as significant potential contributors to Earth surface processes and to climate change. However, there is a general perception that these mechanisms occur on timescales that are too slow to account for events on time scales of  $O(100)$  kyr. The observations that we present here should help to overturn this perception. Throughout the North Atlantic region, there is evidence for repeated transient vertical displacements of the Earth's surface that cannot be accounted for by glacio-eustatic mechanisms. These displacements are indirectly recorded as buried ephemeral landscapes. The best-preserved landscapes share common attributes with hyperthermal events— they occur at the same times, they are geologically rapid,

and they coincide with excursions of gamma ray intensity. We infer that thermal fluctuations of the Icelandic mantle plume played a role in triggering some of these hyperthermal events. Several of these events are characterized by double-spiked excursions which may be hallmarks either of eccentric forcing or of staged uplift events for which there is independent geologic evidence (Hartley et al., 2011).

Our results have far-reaching implications. The Milankovitch hypothesis has, for excellent reasons, provided a superb quantitative framework for interpreting stratigraphic and isotopic records. However, it is becoming clear that tectonic events driven by mantle convective dynamics can intrude upon this rhythmic tempo. The best-known hyperthermal events appear to fall within a long-period climatic oscillation which may itself have been triggered by the two-stage evolution of the Icelandic plume which could have enhanced sensitivity to orbital forcing. The events themselves coincide with, and can be at least partly explained by, episodes of transient landscape development that are linked with short-period fluctuations in plume activity. In conclusion, we suggest that a detailed and integrated multi-disciplinary analysis of the Icelandic plume across a range of spatial and temporal scales should bear fruitful paleoclimatic insights.

#### CRediT authorship contribution statement

**Benedict Conway-Jones:** Conceptualization, Methodology, Investigation, Writing. **Nicky White:** Conceptualization, Methodology, Supervision, Writing.

#### Declaration of competing interest

The authors declare that they have no known competing financial interests or personal relationships that could have appeared to influence the work reported in this paper.

#### Appendix A. Seismic reflection survey

The Faroe-Shetland MegaSurvey was used to identify and to map buried ephemeral landscapes. This seismic reflection survey was generated by Petroleum Geo-Services (PGS) ASA who merged  $> 30$  individual 3D surveys into a single consistent dataset that has an aerial coverage of  $23,652 \text{ km}^2$ . Individual surveys are of variable vintage, orientation and quality. Each survey was interpolated and rebinned onto a standard grid by PGS. Seismic amplitude and two-way travel time were then matched from survey to survey. The integrated dataset was spatially migrated in the time domain. A typical example of an individual survey is that acquired close to the center of the Faroe-Shetland basin by the *PGS Ramform Explorer* between 27 July and 20 August 1997. During acquisition, ship speed varied between  $1.8 \text{ ms}^{-1}$  and  $2.5 \text{ ms}^{-1}$ . The vessel towed two acoustic sources at an average depth of 7.5 m that were separated by 50 m in the cross-streamer (i.e. northwest-southeast) direction. Each source comprised a tuned array of airguns with a total volume 3,090 cubic inches (50.6 l), which was primed with air that had a pressure of 2,000 psi (13.8 Mpa). The two sources were alternately fired every 10–14 s depending upon the speed of the vessel, which corresponds to a distance along the ground of 25 m. Each source generated an acoustic impulse (i.e. source wavelet) that closely approximates a Ricker wavelet with a peak frequency of 30 Hz. This impulse is principally directed downward through the water column and into the solid Earth where it is progressively transmitted and reflected at lithologic boundaries characterized by changes of acoustic impedance. Reflected waves are recorded along eight streamers (i.e. cables of hydrophones), which were each 3.6 km long and towed at an average depth of

9 m. The nominal (i.e. intended) lateral separation between adjacent streamers was 50 m and each streamer had 288 hydrophone arrays that were spaced every 12.5 m. The hydrophone sampling interval was 2 ms. Under optimal conditions, each transect consists of 16 lines that are separated laterally by 25 m. Each of these lines has a nominal fold of cover (i.e. redundancy) of 36. There are many comprehensive accounts of signal processing procedures and of associated terminology available for further consultation.

### Appendix B. Depth conversion, decompaction and isostatic unloading

Checkshot surveys (i.e. downhole measurements of two-way travel time and depth) for 45 boreholes that penetrate the seismic reflection volume were compiled and a local velocity model was constructed by formal least-squares analysis (Shaw Champion et al., 2008). The resultant time-depth relationship takes the form

$$z = V_{ma} \left( \frac{t}{2} + a \exp(bz - 1) \right), \quad (\text{B.1})$$

where  $z$  is depth,  $t$  is two-way travel time,  $a$  and  $b$  are constants with values 0.8871 and  $-0.000434$ , respectively. The solid grain velocity is assumed to be  $V_{ma} = 6 \text{ km s}^{-1}$  (Shaw Champion et al., 2008). Since  $z$  occurs on both sides, Equation (B.1) is solved by Newton-Raphson iteration.

Sedimentary compaction caused by the overlying burden is corrected for using the standard porosity-depth relationship. Porosity,  $\phi$ , as a function of depth,  $z$ , is given by

$$\phi(z) = \phi_o \exp(-z/\lambda), \quad (\text{B.2})$$

where  $\phi_o$  is initial porosity (i.e. at  $z = 0$ ) and  $\lambda$  is the compaction decay length. A sedimentary layer is defined by the flattening surface,  $z_1$ , and by the landscape,  $z_2$ . Conservation of mass requires that

$$\int_{z_1}^{z_2} (1 - \phi) dz = \int_0^{z_3} (1 - \phi) dz, \quad (\text{B.3})$$

where  $z_3$  is the corrected layer thickness at time of deposition. An important corollary is that post-depositional tectonics effects are removed. Integration of Equation (B.3) yields

$$z_3 = z_2 - z_1 + \phi_o \lambda \left( \exp\left(\frac{-z_2}{\lambda}\right) - \exp\left(\frac{-z_1}{\lambda}\right) - \exp\left(\frac{-z_3}{\lambda}\right) + 1 \right). \quad (\text{B.4})$$

Equation (B.4) is solved by Newton-Raphson iteration. We assume a sandstone lithology where  $\phi_o = 0.5$  and  $\lambda = 2.5 \text{ km}$ . Large uncertainties in these compaction parameters do not significantly affect our results. Recovered values of  $z_3$  are subsequently adjusted so that the coastline is placed at  $z = 0$ .

Finally, the regional uplift,  $U$ , recorded by a given landscape is calculated from the observed denudational relief of the landscape,  $D$ . Since the flexural rigidity of the continental shelf of northwest Europe is negligible and since the scale of regional uplift occurs over hundreds of kilometers, it is reasonable to assume Airy isostasy which yields

$$U = \left( \frac{\rho_a}{\rho_a + \rho_s} \right) D, \quad (\text{B.5})$$

where  $\rho_s = 2.65 \text{ Mg km}^{-3}$  is sediment density and  $\rho_a = 3.2 \text{ Mg km}^{-3}$  is asthenospheric mantle density. Calculated values of  $U$  are used to estimate amplitudes of thermal fluctuations.

### Appendix C. Orbital tuning and stratigraphic dating

The relationship between depth and age (i.e. sedimentation rate) in boreholes is determined by biostratigraphic events that are manifest by the First Appearance Datum (FAD) and/or Last Appearance Datum (LAD) of individual marker fossils. Between each biostratigraphic event, sedimentation rate is generally assumed to be constant, despite the fact that even in boreholes with very low sedimentation rates and homogeneous lithologies, rates can vary by up to  $2 \text{ cm ka}^{-1}$  (Barnet et al., 2019). Here, we have tuned gamma ray intensity logs from distal boreholes of the Faroe-Shetland basin with respect to the Fe intensity log from Ocean Drilling Program (ODP) Site 1262 without altering sedimentation rates by more than  $2 \text{ cm ka}^{-1}$ . Given observed biostratigraphic constraints, there is significant coherence between peak gamma ray intensities measured in Faroe-Shetland boreholes and peak Fe intensities measured in Site 1262 at times that correspond to transient landscape development, given acceptable fluctuations in sedimentation rate.

About 20 Paleogene clastic fan deposits from the North Sea basin were originally described and placed within a detailed chronostratigraphic framework by Neal (1996). A subset of these fan deposits was linked with pulsing of the Icelandic plume by White and Lovell (1997). Here, we update the chronostratigraphy of these deposits using a revised and orbitally tuned biostratigraphic framework (Speijer et al., 2020). The oldest fan deposit is Maureen and contains the LAD of *Alisocysta reticulata* which places this deposit at 61.4 Myrs,  $\sim 0.5$  Myrs earlier than proposed by Neal (1996). The LAD of *Isabelidium? viborgense* post-dates the Andrew fan, which places this fan at 60.0 Myrs,  $\sim 1$  Myrs earlier than previously suggested. The Lower and Upper Balmoral fans experience a substantial temporal shift of 1.6–2 Myrs because Speijer et al. (2020) show that the LADs of *Palaeoperidinium pyrophorum* and of *Alisocysta margarita*, which occur above the Lower and Upper Balmoral fans respectively, are 1.9–2.5 Myrs older than proposed by Neal (1996). The Forties-Sele-Balder-Frigg sequence of fan deposits does not shift by more than 0.5 Myrs since the revised zonation of *Apectodinium augustum*, *Wetzelialla astrata*, *Deflandrea oebisfeldensis* and *Dracodinium solidum* together with the corresponding nanoplanktonic zonation are unchanged. In this way, the revised chronostratigraphy of fan deposits presented in Fig. 6c simultaneously honors the biostratigraphic constraints of Neal (1996) and the revised absolute ages of foraminiferal and dinoflagellate zones provided by Speijer et al. (2020).

### Appendix D. Production and decay calculations

If we assume that the production rate of a species,  $c$ , has a Gaussian distribution as a function of time,  $t$ , and a decay rate that is governed by  $\lambda$ , we obtain

$$\frac{dc}{dt} = \exp\left(\frac{-(t - t_o)^2}{a}\right) - \lambda c, \quad (\text{D.1})$$

where  $t_o$  is the time of peak carbon production and  $a = 2\sigma^2$  is the standard deviation of the Gaussian distribution. This ordinary differential equation has an analytical solution given by

$$c = \frac{1}{\exp(\lambda t)} \int_0^t \exp\left(\frac{-(t - t_o)^2}{a} + \lambda t\right) dt. \quad (\text{D.2})$$

It is straightforward to show that

$$c = \frac{\sqrt{\pi a}}{2} \exp\left(\frac{\lambda(4t_o + a\lambda)}{4} - \lambda t\right) \left( \text{erf}\left(\frac{2t - 2t_o - a\lambda}{2\sqrt{a}}\right) \right)$$

$$+ \operatorname{erf}\left(\frac{2t_o + a\lambda}{2\sqrt{a}}\right)). \quad (\text{D.3})$$

The long-period oscillation of  $\delta^{13}\text{C}$  values between 64 and 48 Myrs is fitted by assuming that

$$\delta^{13}\text{C}(t) = \frac{M_i \delta^{13}\text{C}_i + c_v(t) \delta^{13}\text{C}_v + c_s(t) \delta^{13}\text{C}_s}{M(t)}. \quad (\text{D.4})$$

$c_s(t)$  and  $c_v(t)$  are calculated from Equation (D.3) and depend upon the values of  $F_{s,v}$ ,  $\lambda_{s,v}$ ,  $t_{os,v}$  and  $a_{s,v}$ .

Our modeling strategy is divided into two parts. We first calculate the carbon isotopic ratio for silicate weathering as a function of time,  $\delta^{13}\text{C}_s(t)$ , using Equation (D.4). It is assumed that sequestering of carbon mass is approximated by a Gaussian distribution as a function of time calibrated with respect to the distribution of clastic deposition (Neal, 1996). This calibration yields the peak of silicate weathering as  $t_{os} = 58.8$  Myrs with a standard deviation of  $\sigma_s = 1.89$  Myr. Silicate weathering sequesters  $\text{CO}_2$  by carbonate precipitation where  $\delta^{13}\text{C}_s = 0\text{‰}$ . Using a value of zero requires the maximum amount of silicate weathering—a productivity bloom caused by enhanced nutrient delivery would act to increase the value of  $\delta^{13}\text{C}_s$  and, furthermore, enhanced carbonate weathering acts to buffer  $\delta^{13}\text{C}$ . We calculate the carbon isotopic ratio for volcanic outgassing,  $\delta^{13}\text{C}_v(t)$ , in an analogous way. We assume that production of carbon mass is approximated by a Gaussian distribution calibrated with respect to the distribution of magmatism along the plate margins (White and Lovell, 1997; Storey et al., 2007). This calibration yields the peak of magmatism as  $t_{ov} = 55$  Myrs with a standard deviation of  $\sigma_s = 1.44$  Myrs. We assume that  $\delta^{13}\text{C}_v = -11 \pm 2.2\text{‰}$ , which implicitly assumes a degree of augmentation by melting of permafrost and clathrate deposits (Gutjahr et al., 2017).

Note that production and decay of each carbon contribution,  $c_{s,v}(t)$ , also depends upon respective values of scaling factors,  $F_{s,v}$ , and decay constants,  $\lambda_{s,v}$  (Table 1; Appendix). The misfit between observed and calculated histories of  $\delta^{13}\text{C}$  is minimized as a function of these values using a conjugate gradient search algorithm. At the locus of the global minimum, residual misfit between observed and calculated histories of  $\delta^{13}\text{C}$  curve is 0.26 (Fig. 7a; Table 1).

## Appendix E. Supplementary material

Supplementary material related to this article can be found online at <https://doi.org/10.1016/j.epsl.2022.117644>.

## References

- Barnet, J.S.K., Littler, K., Westerhold, T., Kroon, D., Leng, M.J., Bailey, I., Röhl, U., Zachos, J.C., 2019. A high-fidelity benthic stable isotope record of late Cretaceous–early Eocene climate change and carbon-cycling. *Paleoceanogr. Paleoclimatol.* 34, 672–691.
- Beerling, D.J., Royer, D.L., 2011. Convergent Cenozoic  $\text{CO}_2$  history. *Nat. Geosci.* 4, 418–420.
- Bice, K.L., Marotzke, J., 2002. Could changing ocean circulation have destabilized methane hydrate at the Paleocene/Eocene boundary? *Paleoceanogr.* 17, 1–8.
- Brooks, C.K., 2011. The East Greenland rifted volcanic margin. *Geol. Surv. Den. Greenl. Bull.* 24, 96.
- Coccioni, R., Frontalini, F., Catanzariti, R., Jovane, L., Rodelli, D., Rodrigues, I.M.M., Savian, J.F., Giorgioni, M., Galbrun, B., 2019. Paleoenvironmental signature of the selandian–thanetian transition event (STTE) and Early Late Paleocene event (ELPE) in the Contessa Road section (western Neo-Tethys). *Palaeogeogr. Palaeoclimatol. Palaeoecol.* 523, 62–77.
- Colbourn, G., Ridgwell, A., Lenton, T.M., 2015. The time scale of the silicate weathering negative feedback on atmospheric  $\text{CO}_2$ . *Glob. Biogeochem. Cycles* 29, 583–596.
- Dalhoff, F., Chalmers, J.A., Gregersen, U., Nöhr-Hansen, H., Rasmussen, J.A., Sheldon, E., 2003. Mapping and facies analysis of Paleocene–Mid-Eocene seismic sequences, offshore southern West Greenland. *Mar. Pet. Geol.* 20, 935–986.
- Dam, G., 2002. Sedimentology of magmatically and structurally controlled outburst valleys along rifted volcanic margins: examples from the Nuussuaq Basin, West Greenland. *Sedimentology* 49, 505–532.
- Dickson, A.J., Cohen, A.S., Coe, A.L., Davies, M., Shcherbinina, E.A., Gavrillov, Y.O., 2015. Evidence for weathering and volcanism during the PETM from Arctic Ocean and Peri-Tethys osmium isotope records. *Palaeogeogr. Palaeoclimatol. Palaeoecol.* 438, 300–307.
- Frieling, J., Svensen, H.H., Planke, S., Cramwinckel, M.J., Selnes, H., Slujs, A., 2016. Thermogenic methane release as a cause for the long duration of the PETM. *Proc. Natl. Acad. Sci.* 113, 12059–12064.
- Gale, A.S., Lovell, B., 2020. Control of the Paleogene sedimentary record of the Anglo-Paris Basin by both the Iceland mantle plume and the Massif Central hotspot. *Proc. Geol. Assoc.* 131, 652–666.
- Gutjahr, M., Ridgwell, A., Sexton, P.F., Anagnostou, E., Pearson, P.N., Pälike, H., Norris, R.D., Thomas, E., Foster, G.L., 2017. Very large release of mostly volcanic carbon during the Paleocene–Eocene Thermal Maximum. *Nature* 548, 573–577.
- Harper, D.T., Hönisch, B., Zeebe, R.E., Shaffer, G., Haynes, L.L., Thomas, E., Zachos, J.C., 2020. The magnitude of surface ocean acidification and carbon release during Eocene Thermal Maximum 2 (ETM-2) and the Paleocene–Eocene Thermal Maximum (PETM). *Paleoceanogr. Paleoclimatol.* 35, e2019PA003699.
- Hartley, R.A., Roberts, G.G., White, N.J., Richardson, C.N., 2011. Transient convective uplift of an ancient buried landscape. *Nat. Geosci.* 4, 562.
- Hilton, R.G., West, A.J., 2020. Mountains, erosion and the carbon cycle. *Nat. Rev. Earth Environ.* 1, 284–299.
- Jones, M.T., Percival, L.M.E., Stokke, E.W., Frieling, J., Mather, T.A., Riber, L., Schubert, B.A., Schultz, B., Tegner, C., Planke, S., 2019a. Mercury anomalies across the Paleocene–Eocene thermal maximum. *Clim. Past* 15, 217–236.
- Jones, S.M., Hoggett, M., Greene, S.E., Jones, T.D., 2019b. Large igneous province thermogenic greenhouse gas flux could have initiated Paleocene–Eocene Thermal Maximum climate change. *Nat. Commun.* 10, 1–16.
- Jones, S.M., White, N.J., Clarke, B.J., Rowley, E., Gallagher, K., 2002. Present and past influence of the Iceland Plume on sedimentation. *Special Publications*, vol. 196. Geological Society, London, pp. 13–25.
- King, C., 2016. A revised correlation of Tertiary rocks in the British Isles and adjacent areas of NW Europe. In: Gale, A.S., Barry, T.L. (Eds.), *Special Reports*. Geological Society of London, London, pp. 1–716.
- Knox, R.W., Holloway, S., Kirby, G.A., Bailey, H.E., 1997. Stratigraphic Nomenclature of the UK North West Margin. 2. Early Paleogene Lithostratigraphy and Sequence Stratigraphy. British Geological Survey, Nottingham.
- Larsen, M., Hamberg, L., Olausson, S., Nørgaard-Pedersen, N., Stemmerik, L., 1999. Basin evolution in southern East Greenland: an outcrop analog for Cretaceous–Paleogene basins on the North Atlantic volcanic margins. *Am. Assoc. Pet. Geol. Bull.* 83, 1236–1261.
- Lauretano, V., Littler, K., Polling, M., Zachos, J.C., Lourens, L.J., 2015. Frequency, magnitude and character of hyperthermal events at the onset of the Early Eocene Climatic Optimum. *Clim. Past* 11, 1313–1324.
- McInerney, F.A., Wing, S.L., 2011. The Paleocene–Eocene Thermal Maximum: a perturbation of carbon cycle, climate, and biosphere with implications for the future. *Annu. Rev. Earth Planet. Sci.* 39, 489–516.
- Mudge, D.C., Bujak, J.P., 1996. An integrated stratigraphy for the Paleocene and Eocene of the North Sea. *Geol. Soc. (Lond.) Spec. Publ.* 101, 91–113.
- Mudge, D.C., Bujak, J.P., 2001. Biostratigraphic evidence for evolving palaeoenvironments in the lower Paleogene of the Faeroe–Shetland Basin. *Mar. Pet. Geol.* 18, 577–590.
- Neal, J.E., 1996. A Summary of Paleogene Sequence Stratigraphy in Northwest Europe and the North Sea. *Special Publications*, vol. 101. Geological Society, London, pp. 15–42.
- Parnell-Turner, R., White, N.J., Henstock, T.J., Murton, B.J., MacLennan, J., Jones, S.M., 2014. A continuous 55-million-year record of transient mantle plume activity beneath Iceland. *Nat. Geosci.* 7, 914.
- Plink-Björklund, P., Steel, R., 2006. Incised valleys on an Eocene coastal plain and shelf, Spitsbergen-part of a linked shelf-slope system. In: *SEPM Special Publication*, vol. 85, pp. 281–307.
- Pujalte, V., Schmitz, B., Baceta, J.I., 2014. Sea-level changes across the Paleocene–Eocene interval in the Spanish Pyrenees, and their possible relationship with North Atlantic magmatism. *Palaeogeogr. Palaeoclimatol. Palaeoecol.* 393, 45–60.
- Ren, S., Faleide, J.I., Eldholm, O., Skogseid, J., Gradstein, F., 2003. Late Cretaceous–Paleocene tectonic development of the NW Vøring basin. *Mar. Pet. Geol.* 20, 177–206.
- Röhl, U., Norris, R.D., Ogg, J.G., 2003. Cyclostratigraphy of upper Paleocene and lower Eocene sediments at Blake Nose Site 1051 (western North Atlantic). In: *Geological Society of America Special Papers*, vol. 369, pp. 567–588.
- Rudge, J.F., Shaw Champion, M.E., White, N.J., McKenzie, D.P., Lovell, B., 2008. A plume model of transient diachronous uplift at the Earth's surface. *Earth Planet. Sci. Lett.* 267, 146–160.
- Schoonman, C.M., White, N.J., Pritchard, D., 2017. Radial viscous fingering of hot asthenosphere within the Icelandic plume beneath the North Atlantic Ocean. *Earth Planet. Sci. Lett.* 468, 51–61.
- Shaw Champion, M.E., White, N.J., Jones, S.M., Lovell, B., 2008. Quantifying transient mantle convective uplift: an example from the Faeroe–Shetland basin. *Tectonics* 27.
- Shipboard Scientific Party, 2004. Leg 210 summary. In: *Proc. Ocean Drill. Program, Init. Repts., Ocean Drilling Program*. College Station, TX, pp. 1–78.



- Sluijs, A., Brinkhuis, H., 2009. A dynamic climate and ecosystem state during the Paleocene-Eocene Thermal Maximum: inferences from dinoflagellate cyst assemblages on the New Jersey Shelf. *Biogeosciences* 6, 1755–1781.
- Speijer, R.P., Pälike, H., Hollis, C.J., Hooker, J.J., Ogg, J.G., 2020. The Paleogene period. In: Gradstein, F.M., Ogg, J.G., Schmitz, M.D., Ogg, G.M. (Eds.), *Geologic Time Scale 2020*. Elsevier, Amsterdam, pp. 1087–1140.
- Steurbaat, E., King, C., 2017. The composite Kortrijk section (W Belgium): a key reference for mid-Ypresian (Early Eocene) stratigraphy in the southern North Sea Basin. *Geol. Belg.* 20.
- Stoker, M.S., Kimbell, G.S., McInroy, D.B., Morton, A.C., 2012. Eocene post-rift tectonostratigraphy of the Rockall Plateau, Atlantic margin of NW Britain: linking early spreading tectonics and passive margin response. *Mar. Pet. Geol.* 30, 98–125.
- Storey, M., Duncan, R.A., Swisher, C.C., 2007. Paleocene–Eocene thermal maximum and the opening of the northeast Atlantic. *Science* 316, 587–589.
- Stucky de Quay, G., Roberts, G.G., Watson, J.S., Jackson, C.A.L., 2017. Incipient mantle plume evolution: constraints from ancient landscapes buried beneath the North Sea. *Geochem. Geophys. Geosyst.* 18, 973–993.
- Sudermann, M., Galloway, J.M., Greenwood, D.R., West, C.K., Reinhardt, L., 2021. Palynostratigraphy of the lower Paleogene Margaret Formation at Stenkul Fiord, Ellesmere Island, Nunavut, Canada. *Palynology* 45, 1–18.
- Svensen, H.H., Planke, S., Mørth-Sørensen, A., Jamveit, B., Myklebust, R., Eidem, T.R., Rey, S.S., 2004. Release of methane from a volcanic basin as a mechanism for initial Eocene global warming. *Nature* 429, 542–545.
- Westerhold, T., Marwan, N., Drury, A.J., Liebrand, D., Agnini, C., Anagnostou, E., Barnett, J.S.K., Bohaty, S.M., De Vleeschouwer, D., Florindo, F., 2020. An astronomically dated record of Earth's climate and its predictability over the last 66 million years. *Science* 369, 1383–1387.
- Westerhold, T., Röhl, U., Donner, B., Zachos, J.C., 2018. Global extent of early Eocene hyperthermal events: a new Pacific benthic foraminiferal isotope record from Shatsky Rise (ODP Site 1209). *Paleoceanogr. Paleoclimatol.* 33, 626–642.
- White, N.J., Lovell, B., 1997. Measuring the pulse of a plume with the sedimentary record. *Nature* 387, 888.
- White, R.S., McKenzie, D.P., 1989. Magmatism at rift zones: the generation of volcanic continental margins and flood basalts. *J. Geophys. Res., Solid Earth* 94, 7685–7729.
- White, R.S., Smith, L.K., Roberts, A.W., Christie, P.A.F., Kuszniir, N.J., 2008. Lower-crustal intrusion on the North Atlantic continental margin. *Nature* 452, 460–464.
- Wilkinson, C.M., Ganerød, M., Hendriks, B.W.H., Eide, E.A., 2017. Compilation and Appraisal of Geochronological Data from the North Atlantic Igneous Province (NAIP). Special Publications, vol. 447. Geological Society, London, pp. 69–103.
- Zachos, J.C., Pagani, M., Sloan, L., Thomas, E., Billups, K., 2001. Trends, rhythms, and aberrations in global climate 65 Ma to present. *Science* 292, 686–693.